NANO · MICRO small
www.small-journal.com

Understanding Carbon Nanotube-Based Ionic Diodes: Design and Mechanism

*Ran Peng, Yueyue Pan, Biwu Liu, Zhi Li, Peng Pan, Shuailong Zhang, Zhen Qin, Aaron R. Wheeler, Xiaowu (Shirley) Tang, and Xinyu Liu**

The rectification of ion transport through biological ion channels has attracted much attention and inspired the thriving invention and applications of ionic diodes. However, the development of high-performance ionic diodes is still challenging, and the working mechanisms of ionic diodes constructed by 1D ionic nanochannels have not been fully understood. This work reports the systematic investigation of the design and mechanism of a new type of ionic diode constructed from horizontally aligned multi-walled carbon nanotubes (MWCNTs) with oppositely charged polyelectrolytes decorated at their two entrances. The major design and working parameters of the MWCNT-based ionic diode, including the ion channel size, the driven voltage, the properties of working fluids, and the quantity and length of charge modification, are extensively investigated through numerical simulations and/or experiments. An optimized ionic current rectification (ICR) ratio of 1481.5 is experimentally achieved on the MWCNT-based ionic diode. These results promise potential applications of the MWCNT-based ionic diode in biosensing and biocomputing. As a proof-of-concept, DNA detection and HIV-1 diagnosis is demonstrated on the ionic diode. This work provides a comprehensive understanding of the working principle of the MWCNT-based ionic diodes and will allow rational device design and optimization.

1. Introduction

The rectification of ion transport through biological ion channels has gained much attention and inspired the emerging studies of electrokinetic-driven ionic diodes and their applications such as energy harvesting,[1–4] biosensing,[5,6] water desalination,[7] and ionic electronics.[8–11] For example, converting salinity gradients into electric power as high as 3.46 W m^{-2} by using ionic diode membrane has been reported.[12] The label-free detection of femtomolar cardiac troponin by using an integrated nanoslit fluidic diode has also been achieved.[13] In addition, proof-of-concept desalination with 50% efficiency by using a cationic diode was reported recently,[14] and ionic electronics has also boosted the thriving field of wearable electronics. [15] To achieve effective ionic current rectification (ICR), unipolar and bipolar strategies based on the asymmetricity of ion channel properties (i.e., geometry and surface charges) have been reported.[16,17] Over the past decades, a variety of ionic diodes constructed from different nanostructures, including conical nanopores,[16,18–27] hybrid nanomembranes[12,28–39] and nanochannels,[40–44] have been explored; however, the performance of these ionic diodes is not fully satisfactory for many practical applications in fields such as ionic electronics[45,46] and biosensing.[6,47] 1D nanomaterials with natural nanometer-sized tunnels are ideal candidates for engineering ionic diode systems, providing promising routes to the development of high-performance ionic diodes.

Ion transport through carbon nanotubes (CNTs) has been investigated extensively,[49–54] indicating that CNTs have superior intrinsic properties over conventional nanomaterials. For

Dr. R. Peng
Department of Marine Engineering
Dalian Maritime University
1 Lingshui Road, Dalian, Liaoning 116026, China
Dr. R. Peng, Y. Pan, P. Pan, Z. Qin, Prof. X. Liu
Department of Mechanical and Industrial Engineering
University of Toronto
5 King's College Road, Toronto, Ontario M5S 3G8, Canada
E-mail: xyliu@mie.utoronto.ca
Dr. B. Liu, Z. Li, Prof. X. S. Tang
Department of Chemistry & Waterloo Institute for Nanotechnology (WIN)
University of Waterloo
Waterloo, Ontario N2L 3G1, Canada
The ORCID identification number(s) for the author(s) of this article can be found under https://doi.org/10.1002/smll.202100383.
Dr. B. Liu
Institute of Analytical Chemistry and Instrument for Life Science
The Key Laboratory of Biomedical Information Engineering
of Ministry of Education
School of Life Science and Technology
Xi'an Jiaotong University
Xianning West Road, Xi'an, Shaanxi 710049, China
Dr. S. Zhang, Prof. A. R. Wheeler
Department of Chemistry
University of Toronto
80 St. George Street, Toronto, Ontario M5S 3H6, Canada
Dr. S. Zhang, Prof. A. R. Wheeler, Prof. X. Liu
Institute of Biomedical Engineering
University of Toronto
164 College Street, Toronto, Ontario M5S 3G9, Canada

DOI: 10.1002/smll.202100383

instance, the atomic level channel diameter of a CNT is suitable for mimicking real biological ion channels; its superhydrophobic channel wall enables high-efficiency transport of ions and molecules through the CNT; and the super-strong and ultra-long physical properties of CNTs also make them excellent candidates for engineering fluidic devices with complicated structures. In addition, charge modification of the CNT entrances can be readily achieved through physical absorption[55] and covalent conjugation,[56] making it feasible to create asymmetric charge properties on the CNT for ion transport modulation. Pioneering work on CNT-based ionic diodes has been reported by Scruggs et al.[57] and Wu et al.;[58] However, the ICR performance of the reported CNT-based ionic diodes is relatively low, only around 18 and 6, respectively, which is not as satisfactory as that of the ones made from nanomembranes,[12,28–39] because of the large CNT diameter and insufficient charge modification on the CNT entrances. We recently reported a new type of ionic diode created by horizontally aligned multi-walled CNTs (MWCNTs) of ≈5 nm in diameter.[59] A unique feature of this ionic diode design is its batch fabrication process capable of on-chip integration of multiple ionic diodes from the same MWCNT bundle, which has allowed us to form monolithic ionotronic systems including ionic logic gates, ionic rectifiers, and ionic bipolar transistors. In this MWCNT-based ionic diode, cations and anions serve as charge carriers like those of electrons and holes in the semiconductor electronics, and the rectification of ion transport through the MWCNT channel is achieved by decoration of opposite charges on the two CNT channel entrances. In our previous study, we mainly reported the design, fabrication, and integration of ionotronic systems.[59] However, the design parameters and operating conditions of the ionic diode have not been systematically examined, and the optimization of the ICR performance of the ionic diode has not been comprehensively investigated.

This paper presents the modelling, simulation, experimental validation, and design optimization of the MWCNT-based ionic diode, and demonstrates its new application for DNA detection. For ionic diode modelling, Poisson-Boltzmann-Nernst-Plank equations were applied to numerically investigate the key design and working parameters of the MWCNT-based ionic diode, including length and inner diameter of the MWCNTs, the applied voltage, the quantity and length of charge modification on the MWCNT terminals, the ionic concentration of working fluids. Experimental verification and optimization of the ionic diode were performed on batch-fabricated MWCNT ionic diode chips. An ICR ratio as high as 1481.5 was achieved after optimization of the design and working parameters. Finally, a proof-of-concept demonstration of our MWCNT-based ionic diode for DNA detection was also demonstrated.

2. Results and Discussion

2.1. Design and Modelling of the MWCNT-Based Ionic Diode

Our design of the MWCNT-based ionic diode was inspired by biological ion channels and traditional semiconductor diodes, where the transport of charge carriers in a channel structure is modulated by asymmetrically doping the channel with opposite charges. In our design, horizontally aligned MWCNTs serve as ion nanochannels and are asymmetrically modified with polyelectrolytes of opposite charge polarities on the two nanochannel entrances to regulate the mobile ion transport through the MWCNTs. **Figure 1**a schematically illustrates the working principle of the MWCNT-based ionic diode. A MWCNT nanochannel is decorated with positively charged molecule chains poly(diallyldimethylammonium chloride) (PDAC) on its left-side entrance and negatively charged molecule chains poly(styrenesulfonate) (PSS) on its right-side entrance via physical absorption. The transport of mobile ions (K^+ and Cl^- from the KCl solution filled in the left and right side microchannels connecting the MWCNTs) through the nanochannel is gated at the two entrances through electrostatic repulsion/attraction forces generated by the immobilized polyelectrolytes decorated on the MWCNT terminals. For instance, at the left-side channel entrance, the transport of mobile cations is favored while the transport of mobile anions is hampered; at the right-side channel entrance, an opposite gating effect exists. When a forward-biasing electric field is applied on the MWCNT ion channel (from left to right in Figure 1a), the mobile cations in the left reservoir and the mobile anions in the right reservoir are able to migrate through the charge-decorated channel entrances and accumulate inside the MWCNT, giving rise to an enhancement of the ion channel conductivity thus the "ON" state of the ionic diode; when a reverse-biasing electric field is applied (from right to left in Figure 1a), the mobile ions get depleted in the CNT ion channel, resulting in a reduction of the ion channel conductivity and the "OFF" state of the diode. The enhancement and reduction of the ion channel conductivity induce the ICR effect of the ionic diode.

The transport of mobile ions through MWCNT ion channels was simplified and simulated by a 1D symmetric numerical model, as shown in Figure 1b. A MWCNT ion channel of r in radius and L in length (2.5 and 50 nm respectively, unless otherwise stated) bridging two channel reservoirs of R in radius (25 nm, unless otherwise stated) was driven by a direct-current (DC) electric field (V_{app} on AJ and grounded HI). To keep the consistency with our experiments where long polyelectrolyte molecule chains can hardly penetrate and fully occupy the ion channel, in the simulation model the left channel entrance was partially modified with negative charges of σ_{PSS} in density and L_{PSS} in length, and the right channel entrance was decorated with positive charges of σ_{PDAC} in density and L_{PDAC} in length, respectively ($\sigma_{PDAC} = -\sigma_{PSS} = 2\ mC^{-2}$, $L_{PSS} = L_{PDAC} = 5$ nm, unless otherwise stated). The side walls adjacent to the channel entrances were also modified with charges of the same density and polarity as the channel entrances due to the absorption of polyelectrolytes. The transport of ions was modelled by Poisson-Boltzmann-Nernst-Plank equations[57,60,61] thanks to the valid continuity assumption of fluids under the condition of channel size larger than 2 nm in diameter.[62] This condition agrees with the actual situation of our experiments where the MWCNT channels were around 5 nm in diameter (Figure S1b,c: Supporting Information). The governing equations and boundary conditions are listed below.

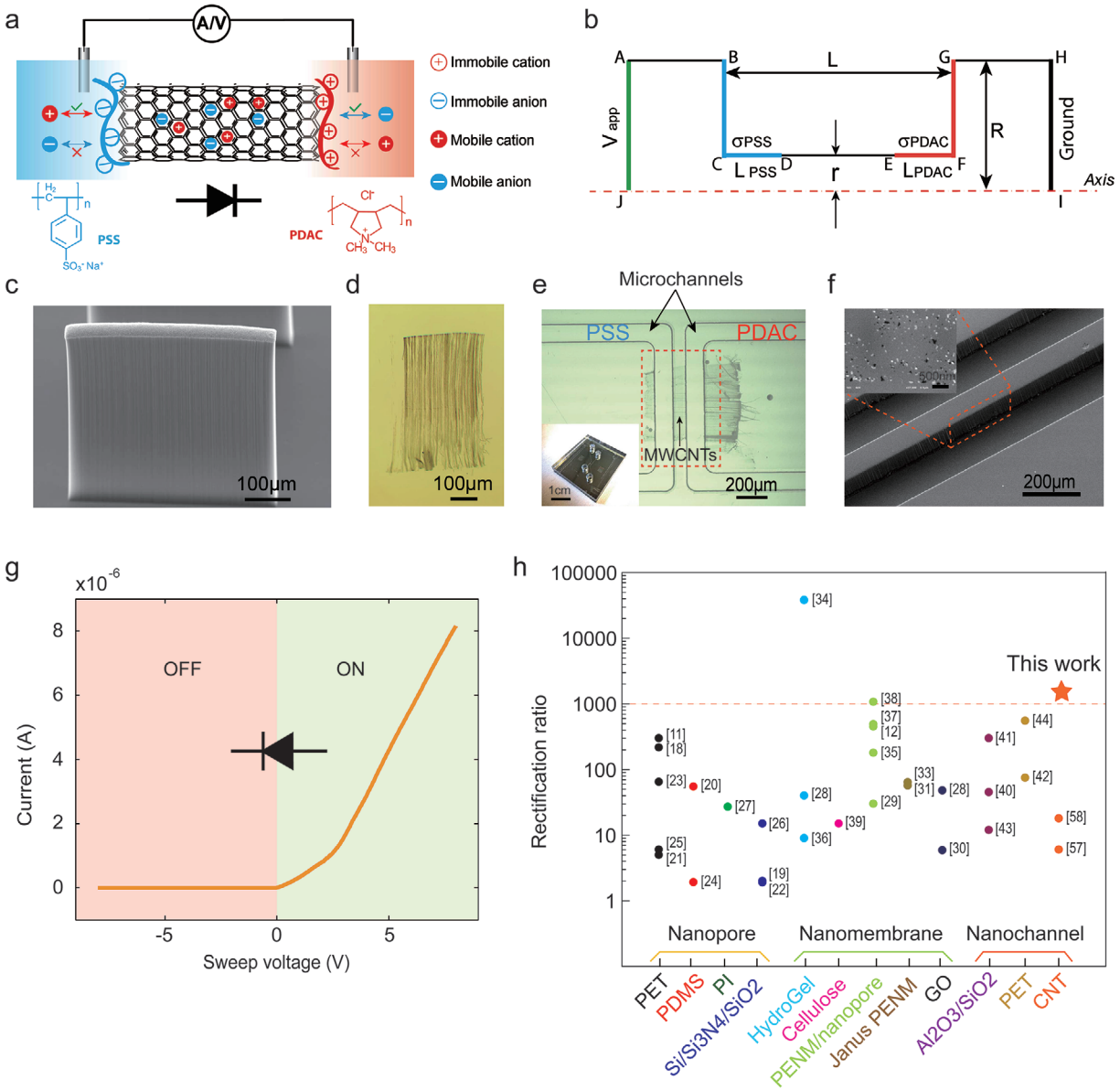

Figure 1. Design, modelling, and fabrication of the MWCNT-based ionic diode. a) Schematic illustration of the ionic diode working principle in which the transport of mobile ions through the MWCNT nanochannel is rectified by the positively charged PDAC and negatively charged PSS molecules decorated on the nanochannel entrances. b) Numerical modelling of the polyelectrolytes-modified ionic diode. c) Scanning electron microscopy (SEM) image of a vertically aligned MWCNT forest synthesized on a silicon wafer by chemical vapor deposition (CVD). d) Optical image of a bundle of horizontally aligned MWCNTs exfoliated from the MWCNT forest. e) Optical image of a nanofluidic chip showing two microchannels bridged by a bundle of MWCNTs. The inset shows a nanofluidic chip after PDMS bonding. f) SEM image of the two microchannels and the SU-8 side wall in between with MWCNTs embedded. The inset shows a zoomed-in view of the embedded MWCNTs after mechanical avulsion. g) The *I*–*V* curve was tested on a MWCNT-based ionic diode with a high ICR ratio of 1148.5 at ±5 V. h) The comparison of the ICR performance of our MWCNT-based ionic diode with that of previous reported ionic diodes constructed based on different nanostructures.

The Poisson equation was applied to solve the electric field in the system:

$$-\nabla\left(\varepsilon_0\varepsilon_r\nabla\varphi\right)=\sigma_e \tag{1}$$

$$\sigma_e = F\sum_i c_i z_i \tag{2}$$

where ϕ, σ_e, and ε_0 are the electric potential, net charge density, dielectric constant of vacuum, respectively, ε_r is the relative dielectric constant of the electrolyte medium, F is the Faraday constant, and c_i and z_i are the concentration and valence of the i^{th} ions, K^+ and Cl^-. A negatively charged condition, σ_{PSS}, was applied on the boundaries BC and CD, and a positively charged condition, σ_{PDAC} was applied on the boundaries EF and FG. The middle part of the MWCNT was left to be electrical neutral which is commonly used in simulations of CNT ion channels.[57] The ion distribution in the computational area was governed by the Nernst-Plank

equation including terms of migration, diffusion, and convection:

$$N_i = -D_i \nabla c_i - z_i \mu_i c_i \nabla \varphi + c_i V_f \quad (3)$$

$$\nabla N_i = 0 \quad (4)$$

where N_i, D_i and $\mu_i = D_i/RT$ are the flux, diffusion coefficient, and ion mobility of K^+ and Cl^-, respectively; and R, T, and V_f are the gas constant, temperature and flow velocity of in the nanochannel system, respectively. Here, we assumed that the concentration of ions at the entrances of the channel reservoirs (AJ and HI) keeps constant, $c_{i\infty}$ (0.1×10^{-3} M, unless otherwise stated), the same as that of the bulk solution. The fluid field was calculated by the Strokes equation and the continuity equation under the conditions of incompressible and laminar flow without pressure applied between the entrances of the channel reservoirs:

$$-\nabla P + \mu \nabla^2 V_f - \rho_e \nabla \phi = 0 \quad (5)$$

$$\nabla \cdot V_f = 0 \quad (6)$$

where P and μ are the pressure and dynamic viscosity of the electrolyte media, and ϕ is the externally applied electric field which was also solved by the Poisson equation. The pressure applied on the entrances of the nanochannels AJ and HI was always zero and non-slip boundary condition was applied on the channel wall DE. The electric field, ionic concentration field and flow field were fully coupled and solved by finite element analysis (FEA) method. Detailed simulation parameters can be found in Table S1 (Supporting Information). The electrical current in the ion channel, I, was finally evaluated by integrating the net charge flux of the mobile ions through the middle cross-section of the nanochannel by

$$I = \int_0^r 2\pi r \left(N_{K^+} - N_{Cl^-} \right) dr \quad (7)$$

Where N_{K^+} and N_{Cl^-} are the flux of K^+ and Cl^-. The performance of the MWCNT-based ionic diode was evaluated by the ICR ratio (Q) under the condition of electric voltages of the same amplitude but opposite polarity, $Q = I(+V)/I(-V)$. The effects of key working parameters, including the channel size, the KCl concentration, the charge density on the nanochannel terminals, the length of charge modification, on the ICR performance (at ±0.5 V, unless otherwise stated) of the ionic diode were systematically studied, as discussed in the following sections. Note that the geometric and working parameters used for numerical simulations were not exactly the same as those in our experiments due to the difficulty in determination of the working parameters of our real cases, including the length of charge modification on the MWCNT terminals, the charge density decorated on the MWCNT entrances etc., and in order to minimize computational load, 50 nm channel length and 5 nm channel diameter were applied in the simulations as an aspect ratio of 10 gives a decent "nanochannel"; however, the simulations demonstrated in this work expand a wide range of values and combinations, which can still provide a comprehensive understanding of the CNT-based ionic diode and give general rules on design and optimization of the CNT-based ionic diodes.

2.2. Fabrication of the MWCNT-Based Ionic Diode

The fabrication of the MWCNT-based ionic diode was described in detail in our previous work.[63] To make this paper self-contained, we briefly introduce the fabrication process here. Vertically aligned MWCNT forest of 500 μm long (Figure 1c) was synthesized on a silicon (Si) wafer by chemical vapor deposition (CVD), and the average inner diameters of the MWCNTs was characterized to be ≈5 nm (Figure S1b,c: Supporting Information). The MWCNT forest was then exfoliated into a bundle of horizontally aligned thin WMCNT membrane (Figure 1d) and embedded into a 55 μm-thick SU-8 photoresist layer spin-coated on a SiO_2-coated Si substrate (Figure S1a-I, Supporting Information). Standard photolithography was applied to pattern two microchannels (separated by 100 μm, unless otherwise stated) on the photoresist layer (Figure S1a-II, Supporting Information), and PDMS-based mechanical avulsion was used to remove the two end portions of the MWCNTs and open their terminals (see Figure S1a-III, Supporting Information). Finally, an enclosed nanofluidic device was obtained by bonding a piece of PDMS punched with inlets and outlets for the two microchannels (Figure S1a-IV, Supporting Information). Figure 1e shows the SU-8 microchannels and the MWCNT nanochannels after mechanical avulsion, and the inset shows the complete nanofluidic device after PDMS bonding. The effectiveness of PDMS-based mechanical avulsion of the MWCNTs was verified by both optical (Figure 1e) and SEM (Figure 1f) imaging. Figure 1f is a zoomed-in SEM image of the red dashed frame in Figure 1e, in which two microchannels are separated by a barrier. MWCNTs are embedded in the channel barrier and bridge the two microchannels. From Figure 1e, one can see that MWCNTs suspended over the microchannels are removed completely. The inset of Figure 1f shows the entrance of the MWCNTs after mechanical avulsion. It is hard to see the hollow channels because the inner diameter of the MWCNTs is too small ≈5 nm. We can only see random "dots" on the surface which indicate the existence of MWCNT channels and based on the width of the dotted area, we can predict the thickness of the embedded MWCNT bundle is ≈2.5 μm. Note that the thickness of the MWCNT bundle is different from chip to chip. Bamboo-like nodes may exist in the MWCNTs due to the deposition of amorphous carbon or catalyst nanoparticles (Figure S2, Supporting Information), which could block the ionic channels of some MWCNTs in the ionic diode. We tested the I–V curve of every chip before the charge modification was performed. Only chips offered apparent ionic current were selected.

2.3. Testing of the MWCNT-Based Ionic Diode

To prepare an ionic diode, PDAC and PSS (1%, unless otherwise stated) diluted in KCl solutions were filled into the two microchannels, respectively. Charge modification on the MWCNT terminals was achieved automatically through

physical absorption (based on electrostatic attraction or π–π interaction[55,64]) of polyelectrolyte molecule chains on the MWCNT terminals. This method is simply by filling the microchannels with evenly dispersed polyelectrolyte-KCl solutions which would result in a dynamic equilibrium of polyelectrolyte decoration on the MWCNT terminals and stable performance of the ionic diode. A linear scanning DC electric field was then applied on the MWCNT nanochannels through platinum (Pt) electrodes to drive the mobile ions, as sketched in Figure 1a. Considering the commonly used operation voltage of solid-state electronics (5 V) and the compatibility of ionic electronics and traditional solid-state electronics, the performance of the ionic diode was evaluated by the ICR ratio (Q) working at ±5 V (unless otherwise stated) experimentally based on the scanning current–voltage (I–V) curve. Here Pt electrodes were used due to their inert and high conductivity properties. Although voltages higher than the minimum potential difference for water electrolysis (≈1.23 V) were applied to the system, the voltage drop mainly occurred on the MWCNT ionic channel due to its ultra-high electrical resistance, the very low current density (≈0.06 A m^{-2}) will not cause significant electrochemical reaction at the interface of electrodes. Figure 1g shows the I–V curve measured on a finally optimized MWCNT-based ionic diode with obvious "ON" and "OFF" states under forward and reverse bias. The forward current at 5 V was measured to be 4 μA and the reverse current at –5 V was 2.7 nA, yielding an ultrahigh ICR ratio of 1481.5. This ICR performance of our MWCNT ionic diode is higher than that of most ionic diodes reported in the literature (usually below 1000), as summarized in Figure 1h where representative ionic diodes developed based on conical nanopores,[16,18–27] nanomembranes[12,28–39] and nanochannels[40–44,57,58] are compared. Note that the ICR ratios collected from these studies are the maximum values as claimed which were obtained under various ionic conditions and in different electric voltage ranges from 0.45 to 10 V (as listed in Table S2, Supporting Information). Based on the data summarized in Figure 1h, we believe that the ICR performance of our MWCNT-based ionic diode is among one of the best ones ever reported.

The ICR effect was also verified by the numerical simulation model. **Figure 2**a illustrates heat maps of the total ionic concentration in the nanochannel when a forward-biasing voltage (1 V) and a reverse-biasing voltage (–1 V) are applied. In this model, a nanochannel of 50 nm long and 5 nm in diameter filled with 0.1×10^{-3} M KCl solution working in the range of –1 to 1 V was simulated. The simulation results clearly show that the mobile ions accumulate in the nanochannel when 1 V voltage is applied (the upper map) and deplete in the nanochannel when –1 V electric voltage is applied (the lower map), giving rise to obvious enhancement and reduction of the channel conductivity and thus the ICR behavior of the ionic diode. For example, in Figure 2b, two I–V curves of the ionic diode,

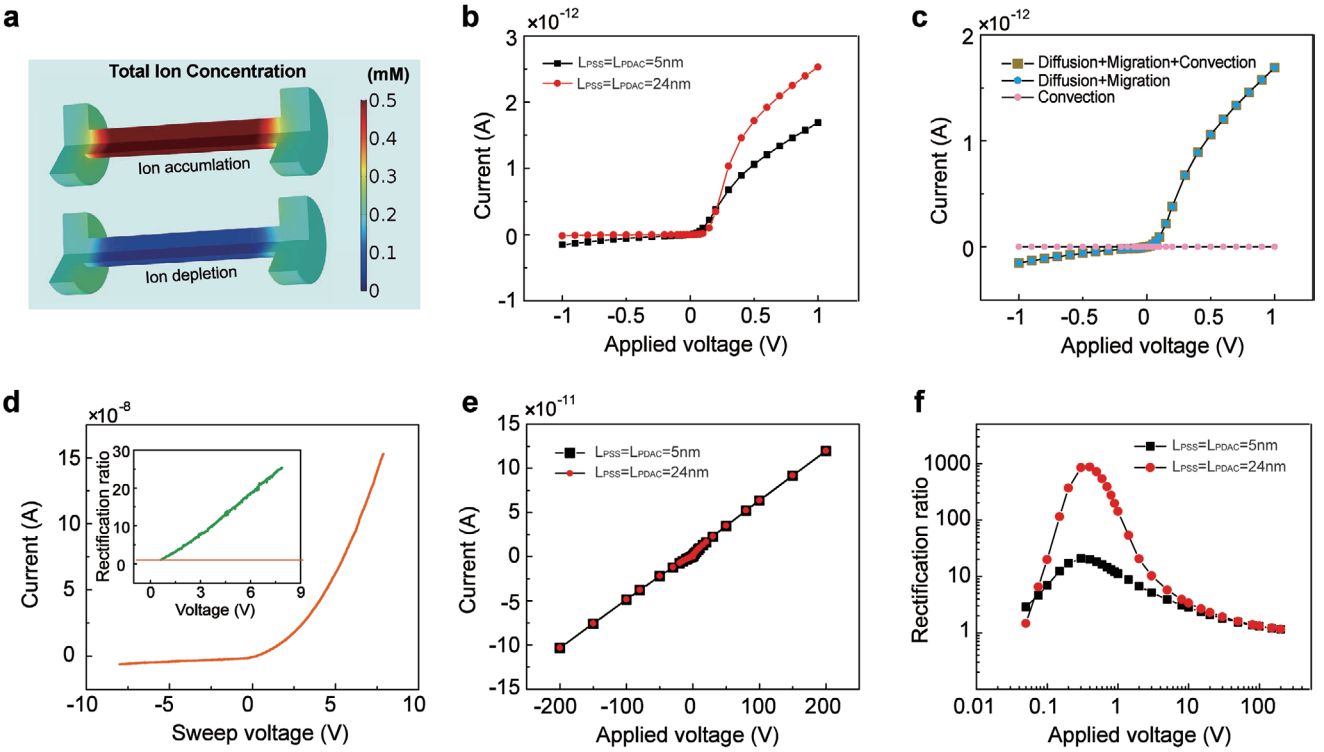

Figure 2. Numerical Simulations of the ICR effect of the MWCNT-based ionic diodes and the effects of applied voltage and electroosmotic flow (EOF) on the ICR performance. a) Simulation results of ion accumulation and depletion in a MWCNT nanochannel when a forward-biasing voltage (upper) and a reverse-biasing voltage (lower) are applied on the ion channel. b) Simulated I–V characteristics of an ionic diode working with charge modification lengths of 5 and 24 nm, in the applied voltage range of –1 to 1 V. c) Components of the total ionic current and contribution of the convection part caused by EOF. d) An experimental I–V curve of an ionic diode and the corresponding ICR ratio (the inset figure). e) Simulation results of an ionic diode working in the range of –200 to 200 V and f) the corresponding ICR ratio.

obtained from numerical simulations with $L_{PSS} = L_{PDAC} = 5$ nm and $L_{PSS} = L_{PDAC} = 24$ nm, show apparent ICR effect. Both the simulation (Figure 2b) and experimental (Figure 1g) results confirm the effectiveness of our ionic diode design for ICR and the reliability of our nanofluidic chips.

2.4. Effect of the Flow Field and the Applied Voltage

The electric current in an ionic diode is initially attributed to the motion of mobile ions, which are specifically driven by three sources: i) diffusion caused by the concentration gradient, ii) migration derived from the electric field, and iii) convection due to the existence of fluid flow (i.e., electroosmotic flow-EOF, V_f). Electroosmotic flows in nanofluidic systems have been investigated extensively;[65–67] however, to the best of our knowledge, no consistent conclusion has been reached about the effect of EOF on the ICR performance of an ionic diode. For example, some researchers argued that the EOF effect is negligible and contributes little to the ionic current due to the comparable ion channel size to the Debye length in a nanofluidic system,[61,68,69] while others claimed that the EOF dominates the rectification behavior of an ionic diode for cases with asymmetric nanochannels of low aspect ratios or nanochannels with highly charged channel walls.[22,26,70,71] Here, we numerically assessed the contribution of the ion convention to the ICR performance of the MWCNT-based ionic diode, by separating the convection term from the other two terms (diffusion and migration) demonstrated in Equation (3). As illustrated in Figure 2c, the contribution of the convection term to the total ionic current is negligible compared to the combined contribution of the other two terms. We believe that this is attributed to the extremely small EOF velocity in the nanochannel due to the overlap of the electric double layer (EDL) and the symmetrical layout of charge modification. For example, the EOF velocity in the ion channel was found, through simulations, to be only around 1 nm s^{-1} under an applied voltage of 0.5 V (Figure S3e,f: Supporting Information). For our ionic diode design, a long nanochannel with its two terminals modified with equal charge modification length and density but opposite polarity, the driving forces for forming the EOFs caused by the two charged terminals are the same in magnitude but opposite in the direction; thus, the EOFs in both directions get canceled in the nanochannel, which explains the low EOF level revealed by our simulations.

The applied voltage also affects the ICR performance of the MWCNT-based ionic diode. Figure 2d shows the experimental data of an *I–V* curve obtained from an ionic diode with an obvious ICR effect, and the inset shows the ICR ratio, extracted from the *I–V* data in Figure 2d, as a function of the applied voltage (at which the ICR ratio is calculated). The ICR ratio increases from ≈1 to ≈25 when the applied voltage changes from ±0.5 to ±8 V. In our simulations, we extended the applied voltage to ±200 V and obtained the *I–V* curves (Figure 2e) in this extended voltage range and the ICR ratio as a function of the applied voltage (Figure 2f). One can see that the ICR ratio increases with the applied voltage in the low voltage range of around ±0.05 V to around ±0.3 V, which agrees with the trend of our experimental data (inset of Figure 2d). However, the simulated ICR ratio decreases with the applied voltage when the voltage is higher than ±0.3 V, thus yielding a maximum ratio value at ±0.3 V for different charge modification lengths (Figure 2f) and KCl concentration (Figure S3d, Supporting Information). This phenomenon was also previously observed in numerical simulations of ionic diodes by Scruggs et al.[57] One possible explanation is the following. Under the condition of a low applied voltage, the charged channel entrances are able to block counterions effectively (i.e., ions deplete in the nanochannel under a reverse-biasing voltage and ions accumulate in the nanochannel under a forward-biasing voltage), and the degree of ion enrichment in the nanochannel increases with the applied forward-biasing voltage. This eventually results in the increase of the ICR ratio with the applied voltage in the low voltage range. However, when the applied voltage exceeds a critical value, the gating of counterions at the entrances becomes less effective or even fails due to the superior migration force (caused by the applied electric field) over the electrostatic repulsion force (resulting from the charged channel entrances on the counterions). Under this situation, the ICR ratio decreases with the applied voltage until the ICR effect fails (where the ICR ratio becomes 1), as shown in Figure 2f. The mechanism of the ICR ratio of an ionic diode decreasing with the applied voltage in the high voltage range is similar to the scenario of "breakdown" in a traditional semiconductor diode. Consequently, an ionic diode can only work properly in a certain voltage range. Note that our experimental result does not show such a peak value of the ICR ratio because of the much longer MWCNT length (100 μm for the diode generating the data in Figure 2d) than the nanochannel length used in our simulations. Based on the experimental data in Figure 2d, it is concluded that our MWCNT-based ionic diode can work properly at least in the range of –8 to 8 V without any degradation of the ICR performance.

2.5. Effect of the Channel Size and the Charge Modification Length

The rectification of ion transport in a nanochannel is essentially achieved by the charge screening effect at the channel entrances which is mainly dominated by both the channel diameter and the concentration of mobile ions. **Figure 3**a shows the simulation results of the effect of channel diameter on the ICR ratio of the MWCNT-based ionic diodes, in which the MWCNT nanochannels ranging from 2 to 30 nm in diameter were evaluated. Apparently, the ICR ratio decreases fast with increasing channel diameter. For example, the ICR ratio of an ionic diode made of nanochannels of 2 nm in diameter is ≈700, and this value decreases to ≈3 as the channel diameter increases to 10 nm; an ionic diode made of a nanochannel of 30 nm in diameter exhibits negligible current rectification behavior, giving an ICR ratio ≈1. Smaller channel diameter gives a higher ICR ratio due to the stronger charge screening effect and the higher-efficient charge gating at the channel entrances; however, when the channel diameter is larger or similar to the Debye length,[72] $\lambda_D = \frac{3.04}{z\sqrt{M}} \times 10^{-10}(m)$ (M is molarity of the symmetrical electrolyte solution), gating of ions at the channel entrances becomes

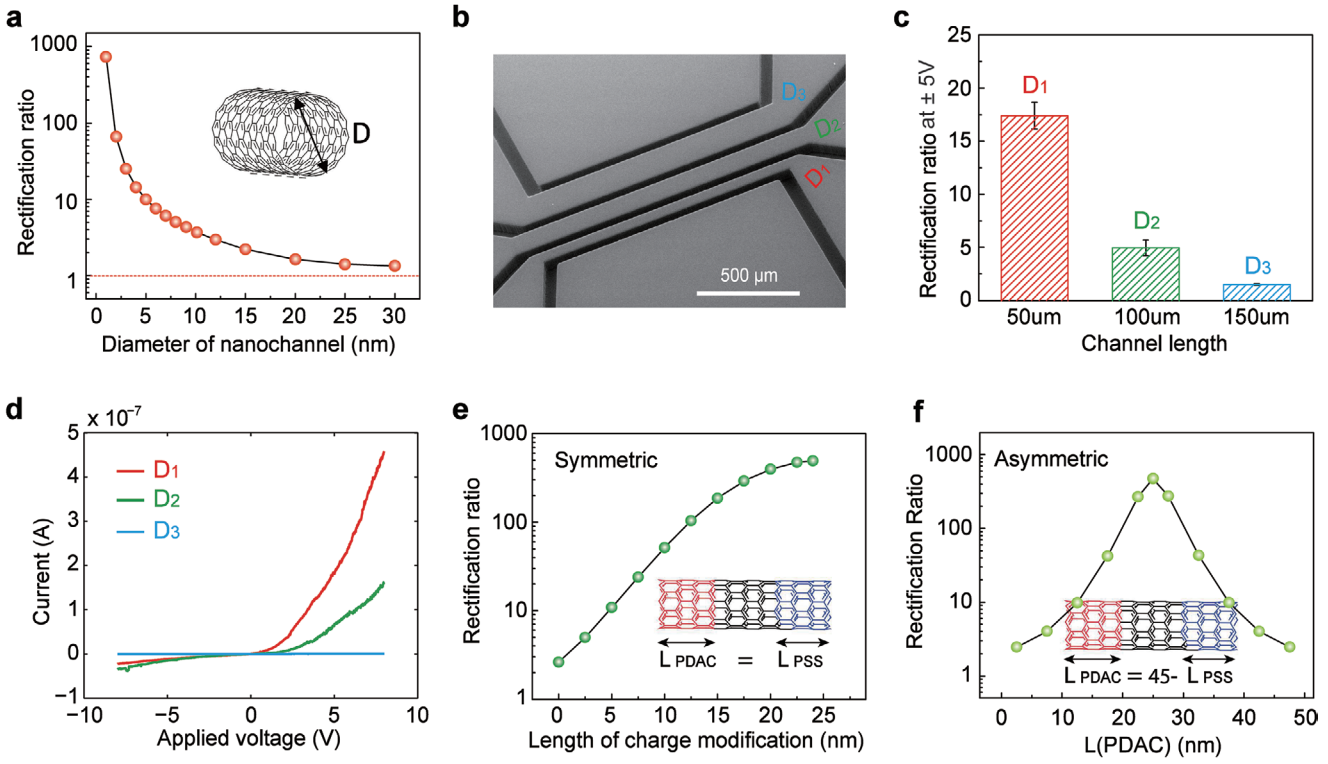

Figure 3. The effects of channel diameter, channel length and charge modification length on the ICR performance of MWCNT-based ionic diode. a) Simulation results of the ICR ratio of the ionic diode as a function of the nanochannel diameter. b–d) Experimental results of the effect of channel length on the ICR performance of the ionic diode. b) An SEM image of a nanofluidic chip constructed with three ionic diodes D_1, D_2, and D_3 with different channel lengths of 50, 100, and 150 μm, respectively. c) Experimental results of channel length effect on the ICR performance of ionic diodes working at ±5 V. d) Examples of typical *I*–*V* curves measured from these three ionic diodes. e,f) Simulation results of charge modification length effects on the ICR performance of the ionic diode, with e) symmetric modification length $L_{PSS} = L_{PDAC}$ and f) asymmetric modification length, $L_{PDAC} = 45\ \text{nm} - L_{PSS}$.

less effective. For example, under the condition of $M = 0.0001$ ($\lambda_D \approx 30$ nm) and 30 nm channel diameter, the insufficient gating effect gives an ICR ratio of only around 1.2, as shown in Figure 3a. A phase diagram of the Debye length and the channel diameter with respect to the ICR ratio can be found in Figure S4 (Supporting Information). One can easily conclude that large channel diameters and collapsing Debye lengths due to increased ionic strength would result in a less effective ion gating effect and ineffective ICR performance. A small channel diameter and a large Debye length would enhance the ICR effect dramatically.

To study the channel length effects, three ionic diodes (denoted by D_1, D_2, and D_3 in Figure 3b) with different channel lengths (50, 100, and 150 μm) were fabricated on one nanofluidic chip by cutting the same bundle of MWCNTs into three sections of different lengths. Fabrication of ionic diodes by the same bundle of MWCNTs ensures the consistency of the ion channel cross-sections of these diodes and the comparability of the ICR performance. The four microchannels were filled with 1% PDAC and 1% PSS diluted in 1×10^{-3} M KCl solution alternately to modify the MWCNT terminals. Figure 3c summarizes the ICR performance of these three MWCNT-based ionic diodes working at ±5 V, showing that the ICR ratio decreases gradually from 17.4 ± 1.2 to 1.5 ± 0.1 (for both $n = 5$) as the channel length increases from 50 to 150 μm. Figure 3d demonstrates typical *I*–*V* curves of these three diodes, indicating that the electric current steeply decreases with increasing channel length which is mainly due to the intuitional increasing resistance of long channels. The experimental result reported here is consistent with the trend of simulation results reported in the literature[60] as well as our simulation results demonstrated in Figure S5a (Supporting Information) (where the ICR ratio decreases with increasing channel length in the relatively long channel range). Our simulation results also predict that the ICR ratio reaches a maximum value at around 200 nm channel length, which is caused by the trade-off of the electrokinetic driven force and the gating repulsion force on the mobile ions at the channel entrances as explained above.

The ICR performance of ionic diodes was previously reported to be affected by the length of charge modification on the ion channels,[57,60,69] but these references mainly focus on the entrance charging effects, under the conditions of fully modified unipolar diodes or fully charged channels with symmetric modification lengths. The observation of partial penetration of fluorescent dye into the MWCNT terminals (see Figure 6d) indicates that long polyelectrolyte molecule chains can hardly fully occupy the entire CNT channel but only migrates into the openings with a certain penetration length, though we did not characterize the exact length of charge modification on the MWCNT terminals at this stage. We investigated the charge modification length effect by numerical simulations extensively. Both asymmetric modification length (Figure 3e)

and asymmetric modification length (Figure 3f) cases were studied in order to fully understand the working mechanisms. In the symmetric case, the nanochannel was modified with PDAC and PSS on either ends of the same length, $L_{PSS} = L_{PDAC,}$ ranging from 0 to 24 nm, while leaving the middle section as electric neutral (as shown in the inset of Figure 3e). The curve in Figure 3e shows that the ICR ratio increases from 2.5 to around 500 as the modification length increases from 0 to 24 nm, suggesting a longer charge modification length gives rise to a better ICR performance of the MWCNT-based ionic diode due to the more effective ion gating effect in longer charged tunnels. A similar conclusion can be obtained from Figure 2b,f in which the performance of nanochannels with 5 and 24 nm modification length is demonstrated. Another nanochannel of the same length but with a larger inner diameter of 7 nm working under the same condition shows a similar increasing trend (Figure S5b, Supporting Information); however, the ICR ratios are lower than those of the 5 nm diameter case, which is caused by the larger inner diameter as discussed in the channel diameter effects section.

Note that the length of the oppositely charged sections may not always identical in real cases due to the variety of polyelectrolyte molecule size and structure and ionic environment et al. For the cases with asymmetric modification lengths, the 50 nm long nanochannel was modified with opposite charges on either end separated by a 5 nm long electric neutral section, i.e., $L_{PDAC} = 45\ nm - L_{PSS}$ (see the inset of Figure 3f). The results summarized in Figure 3f suggest that the rectification ratio reaches its peak at the symmetric point where $L_{PSS} = L_{PDAC} = 22.5$ nm, indicating that a higher symmetricity of charge modification length is favorable to a higher ICR performance of the ionic diode, because a symmetric charge modification length would promise effective gating of both cations and anions at the channel entrances, which also agrees well with the conclusions made in the references.[16,69] Experimental studies on the effect of charge modification length could be achieved by tuning the length of MWCNTs exposed in the microchannels via microfabrication or by using polyelectrolytes of different molecular sizes. For instance, smaller polyelectrolytes penetrate at a longer distance in the MWCNTs compared to larger ones, and thus give rise to a longer charged channel length.

2.6. Effect of the KCl Concentration

Mobile K^+ and Cl^- ions are the main charge carriers in the MWCNT-based ionic diode system, and the concentration of KCl solution in which the polyelectrolytes are diluted is essentially very important to the ICR performance of the device. A numerical simulation of the KCl concentration effect is demonstrated in **Figure 4**a, where the concentration of KCl solutions in both channel reservoirs is in the range of 0.1×10^{-6} м and 1 м. The nanochannel is modified with opposite charges ($\pm 2\ mC^{-2}$) on both terminals of the same length, $L_{PSS} = L_{PDAC} = 5$ nm. Similar cases with a shorter modification length ($L_{PSS} = L_{PDAC} = 0$ nm) or a longer modification length ($L_{PSS} = L_{PDAC} = 24$ nm) can be found in Figure S6a,b (Supporting Information). From the family of curves in Figure 4a, one can see that the ICR ratio increases with decreasing KCl concentration and there are plateaus at both the low-concentration zone and high-concentration zone. It is easy to understand that the ICR ratio approaches 1 at the high concentration zone because of the strong screening of immobile ions at the channel entrances that causing weak ion gating of mobile ions; however, the levelled off saturation of the ICR ratio at the low concentration region is caused by the surface-charge-governed ion transport though nanochannels with heavily overlapped EDL.[41,73,74]

The simulation results were verified by experiments via two typical cases. The first one is a symmetric case where both channel reservoirs were filled with KCl solutions of the same concentration ranging from 1×10^{-6} м to 1 м, all mixed with PSS or PDAC polyelectrolytes. Figure 4b shows the simulation results, and the inset of Figure 4b demonstrates the experimental results showing a similar trend as the simulation results except in the low concentration range. In the experimental data, the decreasing ICR ratio at the low KCl concentration range ($<1 \times 10^{-3}$ м) is caused by extra mobile ions introduced by the PDAC (Cl^-) and PSS (Na^+) polyelectrolytes. In the asymmetric case, the KCl concentration in the left channel reservoir kept constant at 1×10^{-6} м while the KCl solution in the right channel reservoir ramped up from 1×10^{-6} м to 1 м, as sketched in the inset of Figure 4c. Apparently, the ICR ratio decreases with increasing KCl concentration in the right-side reservoir, from 78.6 ± 5.8 to 2.8 ± 0.13 (for both $n = 5$), which agrees with the simulation trend, and regardless of the charge modification length (see the dotted red lines in Figure 4a and Figure S6a,b: Supporting Information). Examples of measured *I–V* curves of the symmetric and asymmetric cases are illustrated in Figure S6c,d (Supporting Information).

It is worth noting that, when the KCl concentration in the left channel reservoir keeps constant at a medium level, a peak value of the ICR ratio may appear as the concentration of KCl in the right channel reservoir ramps up. For example, in Figure 4a, when the left channel reservoir is filled with 1×10^{-3} м KCl solution while the concentration of KCl solution in the right channel reservoir ramps up from 1×10^{-6} м to 1 м, the ICR ratio experiences a hump (denoted by the purple triangular dots) at around 10^{-3} м. The experimental observation could be explained by the charge screening effect and the gating mechanism. For example, when the left side is filled with 1×10^{-3} м KCl solution, the gating effect at the left channel entrance is not effective due to the thin EDL. With the high KCl concentration at the left entrance, even though the concentration of KCl at the right channel entrance is low (e.g., $0.1–10 \times 10^{-6}$ м) to allow effective ion gating, the ICR ratio is still very low (≈1), as shown in Figure S7 (Supporting Information). However, we observe an increase of the ICR ratio with the KCl concentration in the right-side channel, which is caused by the superior ion accumulation effect over ion depletion effect as a forward electric field and a reverse electric field are applied on the channel. From Figure S7 (Supporting Information), one can see that the forward current (ion accumulation) increases faster than the reverse current (ion depletion) when the KCl concentration in the right-side channel increases to 10×10^{-3} м. However, as the KCl concentration in the right side increases further and higher than 10×10^{-3} м, ion gating effect at the right-side channel entrance becomes less effective, and the ICR effect decreases again. As a result, to achieve high ICR performance, the ionic

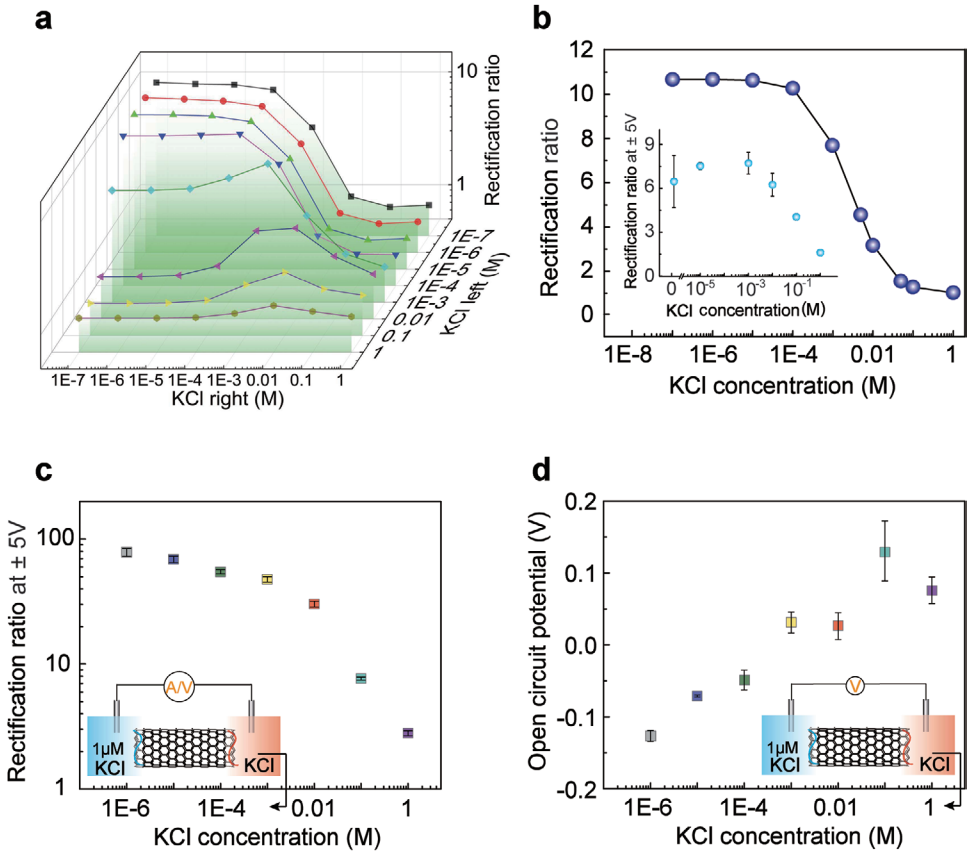

Figure 4. The effect of KCl concentration on the ICR performance of the MWCNT-based ionic diode. a) Numerical simulation results of KCl concentration effects on the performance of the MWCNT-based ionic diode with 5 nm long charge modification on the terminals. b) Simulation results and experimental results (the inset figure) of MWCNT-based ionic diodes working with symmetric KCl concentration in the channel reservoirs. c) Experimental results of a MWCNT-based ionic diode working with asymmetric KCl concentration in the two channel reservoirs. The left side channel reservoir was filled with 2% PSS diluted in 1×10^{-6} M KCl solution and the right-side reservoir was filled with 2% PDAC diluted in KCl solutions ranging from 1×10^{-6} M to 1 M. d) Osmotic potential (open circuit potential) of the MWCNT-based ionic diode filled with asymmetric concentration of KCl solutions.

diode should work with weak ionic strength on both sides to ensure effective ion gating at both channel entrances. We also measured the reversal potential (open circuit potential or OCP) of the asymmetric systems which reveals the asymmetric ion transport through the MWCNTs. As shown in Figure 4d, when the left channel reservoir was filled with 1×10^{-6} M KCl solution mixed with 2% PDAC and the right channel reservoir was filled with KCl solutions ramping from 1×10^{-6} M to 1 M containing 2% PSS, the OCP increases gradually from around –120 mV to about 100 mV, suggesting that the newly designed MWCNT-based ionic diode can be also applied to develop CNT channel-based osmotic nanogenerators for nanoelectronics,[31,75,76] besides the applications based on the ICR phenomenon.

2.7. Effect of the Charge Modification on MWCNT Terminals

Transport of mobile ions through MWCNT channels is gated by the charged terminals while the gating efficiency is mainly dominated by the charge density decorated on the MWCNT terminals, (or equivalently, the concentration of polyelectrolytes mixed in the KCl solutions in our experiments). **Figure 5** shows the investigation of the charge density effect on the ICR performance of the ionic diode by numerical simulations (Figure 5a) and the polyelectrolyte concentration effects by experiments (Figure 5b–f). In the numerical simulation models, positive charges (σ_{PDAC}) and negative charges (σ_{PSS}) in the range of 1 μC m^{-2} to 10 mC m^{-2} were applied to the channel terminals ($L_{PDAC} = L_{PSS} = 5$ nm). Numerical simulation results with a shorter modification length can be found in Figure S8a (Supporting Information). From the family of curves in Figure 5a and Figure S8a (Supporting Information), one can see that for the asymmetric cases where the MWCNT channel is modified with a fixed density of negative charges on one side and varying densities of positive charges on the other side, the ICR ratio increases with the positive charge density gradually. For the symmetric case in which both the MWCNT terminals are modified with opposite charges of the same density, the ICR ratio increases from around 1 to almost 10 000 when the charge density increases from ±1 μC m^{-2} to ±10 mC m^{-2} (Figure 5b). The inset of Figure 5b presents experimental results of a symmetric case where the two channel reservoirs were filled with PDAC and PSS of the same concentration ranging from 0% to 2% v/v and both diluted in 1×10^{-3} M KCl solution. The ICR

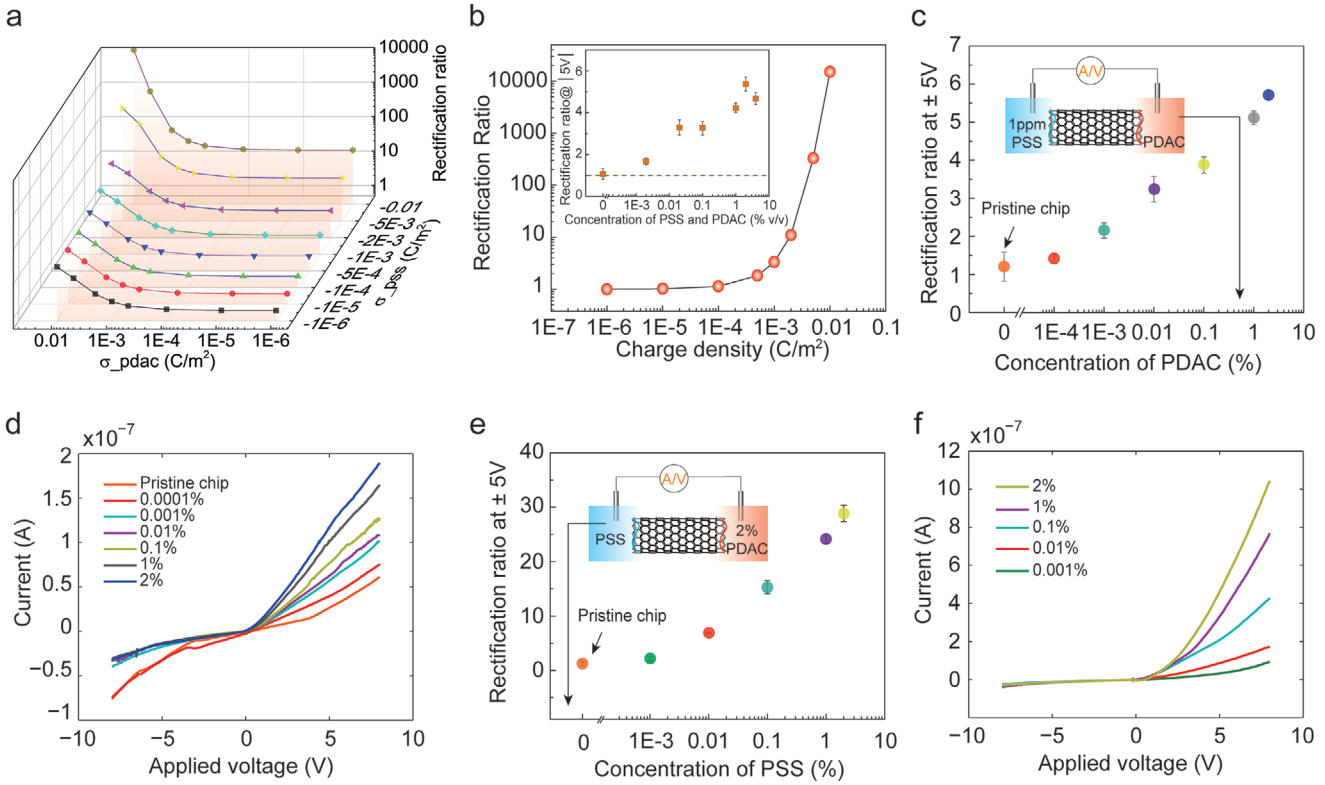

Figure 5. Effects of charge density and polyelectrolyte concentration on the ICR performance of the MWCNT-based ionic diode. a) Numerical simulation results of charge modification effects on the performance of the ionic diode. b) Numerical simulation results of the ionic diode working with symmetric charge density modification and experimental results of a diode working with symmetric concentration of polyelectrolytes. c) Experimental results of the ICR performance and d) a family of *I*–*V* curves of an ionic diode working with asymmetric concentration of polyelectrolytes with 1 ppm PDAC in the left channel reservoir and PDAC in the right channel reservoir ranging from 0.0001% to 2%. e) Experimental results of the ICR performance and f) a family of *I*–*V* curves of an ionic diode working with asymmetric concentration of polyelectrolytes where the right channel reservoir was filled with 2% PDAC and the left channel reservoir was filled with PSS ranging from 0.001% to 2%.

ratio increases with the polyelectrolyte concentration from 1.1 ± 0.2 to 4.7 ± 0.3 (n = 5 for both). Representative experimental *I*–*V* curves are demonstrated in Figure S8b (Supporting Information). We believe that the inconsistency between the experimental results and the simulation results is caused by the discrepancy of parameter selection in the simulation models such as the charge density at the channel terminals and uniformity of the channel size, as mentioned above. For instance, in our experiments, the charge density on the MWCNT terminals may hardly reach 10 mC m^{-2} due to the limited charge bonding sites on the MWCNT terminals.

Experimental results of the asymmetric cases are demonstrated in Figure 5c–f. A MWCNT-based ionic diode was filled with a low and fixed concentration of 1 ppm PSS in the left channel reservoir and PDAC solutions in the right channel reservoir varying from 1 ppm to 2%, as shown in the inset of Figure 5c. The ICR ratio increases from 1.4 ± 0.13 to 5.7 ± 0.12 (n = 5) as the concentration of PDAC increases from 1 ppm to 2%, which is quite different from that of the pristine chip without PDAC modification (around 1.3), as shown in Figure 5c. Typical *I*–*V* characteristics of this asymmetric case are presented in Figure 5d. Apparently, the forward electric current increases with the concentration of PDAC solution, and the reversed current (absolute value) decreases gradually with increasing concentration of the PDAC. The increasing forward current and decreasing reversed current with the concentration of PDAC are caused by the increasing ion gating effect at the right channel terminal (Figure 5d). However, less effective gating of ions at the left channel terminal modified with a low concentration of PSS gives rise to the low ICR performance of the whole device.

We also tested another asymmetric case with one channel reservoir filled with a fixed high concentration of polyelectrolyte to avoid the insufficient ion gating at that terminal and increased the concentration of polyelectrolyte solution on the other side. The inset of Figure 5e shows the experimental setup. A MWCNT-based ionic diode was filled with a high and fixed concentration of 2% PDAC in the right channel reservoir, while PSS solution in the left channel reservoir ramped up from 0.001% to 2%. One can clearly see that the ICR ratio increases dramatically with the concentration of PSS in the left channel reservoir, from 1.2 ± 0.4 to 28.9 ± 1.5 (n = 5), as shown in Figure 5e. The testing *I*–*V* curves in Figure 5f also indicate that the reversed ionic current decreases gradually with the concentration of PSS in the left reservoir, and the forward current increases dramatically with the concentration of PSS in the left reservoir, due to the effective interactions at the left channel entrance as explained above. Based on the results demonstrated

in Figure 5, one can get the ICR ratio of MWCNT-based ionic diode increases with the concentration of polyelectrolyte solutions or the density of change modification on the channel terminals.

According to the results of the numerical simulations and experiments, the general design guidelines for optimizing the ICR performance of a MWCNT-based ionic diode are summarized as follows: i) using CNT/MWCNT channels with shorter length and smaller inner diameter; ii) driving the chip with an appropriate applied voltage; iii) using a proper concentration of ionic solution as the working fluid; iv) modifying the MWCNT entrances with a higher concentration of polyelectrolyte solutions. In addition, the efficiency of charge modification on MWCNT terminals is also affected by the ionic strength and pH of the working solutions. For instance, a neutral pH gives superior ICR performance than other acid or alkaline solutions based on our experimental record (Figure S8c, Supporting Information).[59] An example of the optimized ionic diode is demonstrated in Figure 1g, in which an ionic diode fabricated by shorter MWCNTs of 50 μm modified with 2% PDAC and PSS mixing in 1×10^{-3} M KCl solution of pH ≈7 was tested, and an ICR ratio of 1481.5 was obtained under the condition of ±5 V applied voltage. Note that the chip filled with polyelectrolyte solutions was sealed with a piece of Scotch tape and left at room temperature for 24 h before testing. The long conditioning time enables stable charge modification on the MWCNT terminals and allows for sufficient penetration of polyelectrolyte molecule chains into the MWCNT channels, giving rise to a high charge density, a small channel diameter and a long charge modification length. All these three factors would significantly boost the ICR performance. However, the charge modification process might be significantly accelerated by the electric field-induced self-assembly strategy developed recently.[77] In addition to charge modification, the repeatability of high-performance ionic diodes is heavily dominated by the uniformity of MWCNT channels. CNTs with uniform and small inner diameters are favorable to the high-performance of ionic diodes as mentioned above. We believe that more stable and higher performance of the ionic diode can be constructed by further tuning these working factors and taking the advances of nanofabrication techniques in the future, such as by using catalyst nanoparticles of the same size so that the CNTs synthesized by CVD method would have the same diameter, and by fabricating ultra-long CNTs so that multiple diodes can be fabricated by using the same CNTs.

The apparent changes in ICR ratio with the concentration of polyelectrolytes discussed above suggest that the MWCNT-based ionic diode can work as an excellent platform for sensing polyelectrolyte-based targets. As a typical branch of polyelectrolytes (polyanions), DNA molecules share similar physical properties with PSS, including long immobile molecule chains and the charging philosophy. The flexible functionalization and packaging strategies of DNAs also enable their applications in biosensing and disease diagnosis.[56,78] However, little progress has been updated in the aspect of biosensing using CNT-based ionic diodes. In the following section, a proof-of-concept application of MWCNT-based ionic diodes for DNA detection is demonstrated.

2.8. Demonstration of MWCNT-Based Ionic Diode for DNA Detection

Figure 6a sketches the working mechanism for DNA detection using our MWCNT-based ionic diode and a well-recognized DNA fragment as the biomarker for HIV-1 testing.[79] Following the working steps in Figure 6a, MWCNTs were pretreated and functionalized with carboxylic groups on both terminals. Thereafter, the left terminal was modified with positively charged PDAC molecules (2% in 0.5 × PBS (phosphate-buffered saline)) by physical absorption and the right terminal was functionalized with capture DNA molecules (5'-ACA GAC GGG CAC ACA CTA CT-NH_2-3', 5×10^{-6} M) by EDC (1-ethyl-3-(3-dimethylaminopropyl) carbodiimide hydrochloride/sulfo-NHS (N-Hydroxysulfosuccinimide sodium salt) initialization followed by conjugation of the capture DNA. Electrical characterization was conducted to evaluate the ICR ratio of the MWCNT ionic diode working with 0.5 × PBS solution. Hybridization of the target DNA of HIV-1 (5'-AGT AGT GTG TGC CCG TCT GTT GTG TGA CTC TGG TAA CTA GAG ATC CCT CAG AC-3'6-FAM, 10×10^{-6} M) was achieved by filling the target DNA solution into the right channel reservoir followed by washing. The ICR ratio of the device was measured for the second time under the same ionic condition of 0.5 × PBS environment and compared with the previous measurement without target DNA hybridization. Hybridization of target DNA on the CNT terminal was also verified by monitoring the channel barrier area (the dashed rectangular in Figure 6b) before (Figure 6c) and after (Figure 6d) filling of target DNA in the right microchannel with a fluorescent microscope. Obviously, both edges of the channel barrier are lackluster before target DNA conjugation (Figure 6c); however, the right-side edge of the channel barrier is much brighter than the left side after conjugation of target DNA (Figure 6d), indicating the success of DNA hybridization on the right side of MWCNT terminal. After hybridization of the target DNA, the quantity of negative charges on the right side of the MWCNT channel terminal increases dramatically because the target DNA is much longer than the capture DNA, which would result in an enhancement of the ICR performance of the WMCNT ionic diode. Figure 6e demonstrates typical *I*–*V* curves of the MWCNT ionic diode before and after target DNA hybridization, and Figure 6f summarizes the corresponding ICR performance of the MWCNT ionic diode, indicating that the ICR ratio increases from 12.5 ± 0.7 (n = 10) to 22 ± 1.4 (n = 6) and gives a positive testing result. From both Figure 6e,f, one can get that the newly designed MWCNT-based ionic diode is able to detect the selected DNA marker for HIV-1 testing.

The DNA sensor developed in this work can directly transduce hybridization events into a measurable electronic read-out signal which is straightforward. Multiple ionic diodes on one microfluidic chip would enable multiplexed detection and dehybridization of capture DNA-target DNA couples and recovery of the sensors through microfluidic operations would potentially lower the testing cost. However, here we just show a proof-of-concept demonstration of the ionic diode working as a biosensor based on the concentration effect study. To make the MWCNT-based ionic diode more practical for DNA-based disease diagnosis, high-quality MWCNTs with more uniform and smaller inner diameters are needed to enhance the reliability and

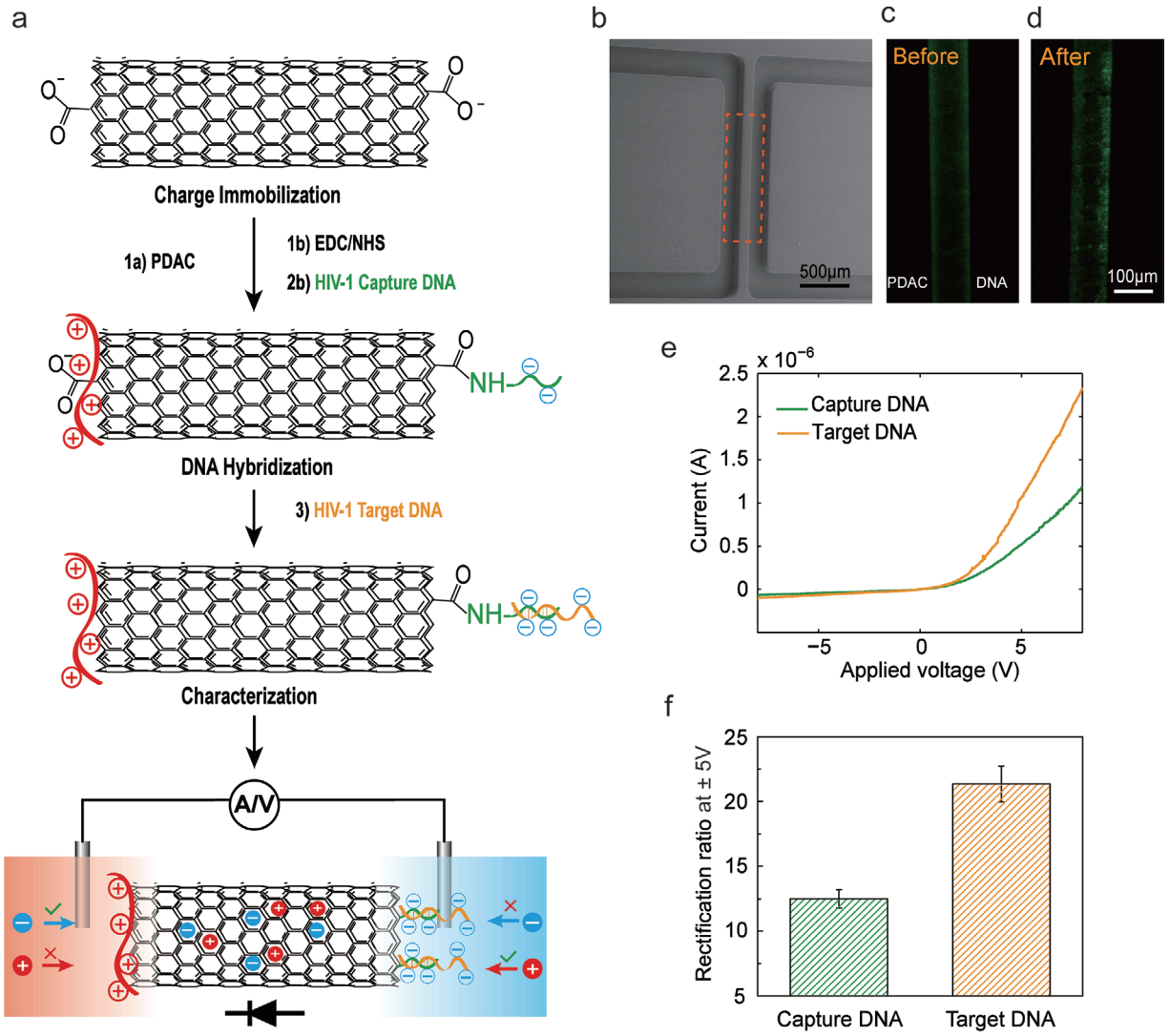

Figure 6. Demonstration of the MWCNT-based ionic diode for DNA detection. a) Schematics of terminal functionalization and DNA detection of the MWCNT-based ionic diode. b) SEM image of the nanofluidic chip. c,d) Fluorescent images of the channel barrier area (dashed rectangular area in the (b)) before and after target DNA hybridization. e) Typical *I–V* curves of the nanofluidic chip before and after target DNA hybridization. f) ICR ratio (at ±5 V) of the MWCNT-based ionic diode before and after target HIV-1 DNA hybridization.

sensitivity of the DNA detection. Systematic investigation of the biosensing system will be performed in our follow-up work.

3. Conclusions

In this article, the MWCNT-based ionic diode was systematically investigated by both experiments and numerical simulations. A potential application of the ionic diode for DNA detection was also demonstrated. The ionic diode was developed on horizontally aligned MWCNT nanochannels by modifying the CNT channel terminals with oppositely charged polyelectrolytes, and an ICR ratio of 1481.5 was achieved which is higher than that of most reported ionic diode systems. The numerical simulation results show that the ICR performance of the MWCNT-based ionic diode is affected by several key working parameters including the channel size, amplitude of the driven electric field, charge density modified on the MWCNT terminals, symmetricity of charge modification lengths, and ionic strength of the working fluids. The effects of the channel length, the concentration of working fluids, and the concentration of polyelectrolytes on the ICR performance of the ionic diode were also investigated experimentally, and the results well agree with the trends of the simulation results. Both simulation and experimental results indicate that the ICR ratio of the MWCNT ionic diode increases with decreasing channel length, decreasing KCl concentration and increasing polyelectrolyte concentrations, providing useful design guidelines for the design and fabrication of high-performance MWCNT-based ionic diodes and the applications thereof. As a proof-of-concept demonstration, a prototype device was developed based on the MWCNT-based ionic diode for the detection of a DNA biomarker for HIV-1 diagnosis. This paper provides a novel strategy to develop high-performance ionic

diodes based on CNT materials as well as general guidelines for designing 1D nanochannel-polyelectrolyte-based ionic diodes. This new ionic diode system could open up a new avenue for ionotronics and chemical/biosensing.

4. Experimental Section

Synthesis and Characterization of MWCNTs: Vertically aligned MWCNTs on silicon wafers were synthesized by chemical vapor deposition (CVD) method as reported previously.[80] Fe nanoparticles were seeded on silicon wafers and patterned by photolithography method to serve as catalyst for CNT synthesis. Briefly, 20 nm thick aluminum oxide layer was deposited on Si wafers by atomic layer deposition. A 4 nm thick Fe film was deposited on the alumina surface by e-beam evaporation and patterned by the lift-off method. The alumina layer works as a diffusion barrier and mediates the surface mobility of Fe and thus promotes the formation of the catalyst particles. Then, ethylene (acting as the carbon source), argon, and hydrogen were passed through a furnace tube of 25 mm in diameter at 725 °C to synthesize the MWCNTs. The length of the MWCNTs used in this study was 500 µm–1 mm long, which was controlled by the synthesis duration. The diameter of the MWCNTs was controlled by the Fe particle size or the thickness of the Fe layer. The diameter and quality of the MWCNTs were characterized by HR-TEM and Raman spectroscopy, indicating that MWCNTs were around 5 nm in diameter (see Figure S1b,c,f: Supporting Information). The MWCNT forests were unrooted by a razor and exfoliated by Scotch tapes into thin bundle membranes thereafter for the following fabrication steps.

Fabrication of MWCNT Ionic Diodes: MWCNT nanofluidic chips were fabricated by following the working protocols developed in the literature,[63] as briefly illustrated in Figure S1a (Supporting Information). A bundle of MWCNTs exfoliated from the CNT forest was transferred onto a 5 µm thick fresh spin-coated SU8 photoresist followed by another round of spin coating of 50 µm thick photoresist. The MWCNTs were embedded in the photoresist (Figure S1a-I, Supporting Information). Standard photolithography procedures including UV exposure and wet developing were applied to generate two microchannels on the photoresist layer for sampling (Figure S1a-II, Supporting Information). After developing, the terminals of the MWCNTs were suspended in the open microchannels. To trim the residual parts of the MWCNTs and open the terminals, a mechanical avulsion method was applied. Briefly, fresh PDMS precursor (10:1) was degassed and cast in the microchannels followed by heating at 85 °C for 1 h. The residual MWCNTs were cast into the PDMS material tightly after curing of the PDMS. Thoroughly peeling off the PDMS slab from the substrate would trim the MWCNTs, as shown in Figure S1a-III (Supporting Information). Finally, a piece of PDMS slab (≈3 mm thick) punched with channel reservoirs was bonded on the substrate after plasma treatment for 30 s (Figure S1a-IV, Supporting Information). Adjusting the level of fluid in the channel reservoirs would promise the stability of ion distribution at the MWCNT channel entrances.

DNA Detection Protocols: HIV-1 DNA detection on the MWCNT-based ionic diode was conducted in several steps. The two microchannels of the nanofluidic chip were filled with HNO_3 (1 M) and H_2O_2 (70%) mixture (1:1) for 30 min to improve the wettability of the MWCNT terminals and to generate –COOH groups on the terminals followed by flushing with DI water for several times to remove the residual acid. Chip conditioning was conducted by filling the left channel with PDAC solution (2%, diluted in 0.5 × PBS, pH 7.4) and the right channel with MES buffer (0.1 M, pH 5.5) for 5 min. Then fresh prepared MES buffer (0.1 M containing 10×10^{-3} M EDC and 20×10^{-3} M sulfo-NHS) was filled into the right channel and incubated for 25 min. After activation, the right-side channel was flushed by MES buffer (0.1 M) and incubated with 5×10^{-6} M capture DNA (5'-ACA GAC GGG CAC ACA CTA CT-NH_2-3') prepared also in 0.1 M MES for overnight. The capture DNA was covalently bonded onto the right side MWCNT channel terminals. A final washing of the right-side channel with MES buffer (0.1 M) and PBS buffer (0.5 ×, pH 7.4) in sequence was conducted to remove residual chemicals and capture DNA from the microchannel. Target DNA for HIV-1 testing (5'-AGT AGT GTG TGC CCG TCT GTT GTG TGA CTC TGG TAA CTA GAG ATC CCT CAG AC-3'6-FAM, 10×10^{-6} M) was prepared in the same PBS buffer (0.5 × PBS pH7.4) and filled into the right-hand side microchannel for 10 min to achieve DNA hybridization. The nanofluidic chip was ready to test after refreshing the left microchannel with PDAC (2% diluted in 0.5 × PBS) solution and the right channel with also 0.5 × PBS.

Data Characterization and Processing: MWCNT nanofluidic chips after conditioning were filled with working solutions and electric fields were applied on the MWCNT nanochannels through channel reservoirs and Pt electrodes. Before each testing, the device was reset by new working solutions for at least 5 times to remove residuals from the last round of testing and to avoid any contaminations. During *I–V* curve characterization, repeatedly bidirectional scanning at 100 mV s^{-1} in the range of –8 to 8 V was applied through all the experiments. Ionic current rectification ratio of *I–V* curves was calculated by using the current values at ±5 V. For the KCl concentration effects and polyelectrolyte concentration effects, working fluids were pumped into the channels from low concentration to high concentration gradually on the same chips and representative data were acquired from the same chip for each parameter study. All the experiments were conducted on different chips at room temperature of 23 °C to assure the reproductivity of the results.

Chemical Reagents and Instruments: Numerical simulation was performed on Comsol 5.3 platform (COMSOL Inc., Burlington, MA). KCl solutions were prepared by dissolving KCl powder (Fisher Scientific) into deionized (DI, pH 8) water. Polyelectrolyte solutions were prepared by diluting Poly(diallyldimethylammonium chloride) (PDAC) (Mw ≈ 400 000, 20 wt% in water, Sigma Aldrich) or poly(sodium 4-styrene-sulfonate) (PSS) (Mw ≈ 7 000 000, 30 wt% in water, Sigma Aldrich) in KCl solutions or phosphate-buffered saline (PBS, Sigma Aldrich) solution. Photolithography on oxidized (300 nm thick, Bruce Technologies Oxidation Furnace) silicon wafers (University Wafer) was conducted by using SU-8 photoresists (SU-8 2005 and 2075, MicroChem) and photo masks (CAD/Art Services, Inc.) with the help of a mask aligner (OAI model 30). Bonding of nanofluidic chip was achieved by treating both the photoresist channels and the PDMS slabs with plasma (Corona SB, SoftLithoBox). MWCNTs were synthesized by CVD (Thermal Fisher) and exfoliated by Scotch tapes (3M) and characterized by optical microscope (Motic, BA 310), SEM (Hitachi-SU3500, JEOL-6610LV and FEI Quanta FEG 250), and high-resolution transmission electron microscopy (HR-TEM) as well as Raman spectroscopy (Horiba Jobin Yvon LabRam 800hR spectrometer with a synapse CCD detector). Capture DNA and target DNA were purchased from IDT (Integrated DNA Technologies) and used as received. EDC (1-ethyl-3-(3-dimethylaminopropyl) carbodiimide hydrochloride (ThermoFisher Scientific) and sulfo-NHS (N-Hydroxysulfosuccinimide sodium salt) (Sigma Aldrich) were applied in the covalent conjugation between the MWCNT and the capture DNA. MES (2-(N-morpholino) ethanesulfonic acid) (BioShop), HNO_3 (Sigma Aldrich) and H_2O_2 (Sigma Aldrich) were diluted in DI water for the desired purposes. DNA hybridization was confirmed by a fluorescent microscope (Nikon Eclipse Ti) and images were captured by NIS-Elements.

Supporting Information

Supporting Information is available from the Wiley Online Library or from the author.

Acknowledgements

The authors acknowledge the financial support from the Natural Sciences and Engineering Research Council of Canada (Grant #RGPIN-2017-06374 and #RGPAS-2017-507980), from the Canada Foundation for Innovation (Grant #JELF-37812). Ran Peng woud like to acknowledge the Fundamental Research Funds for the Central Universities (#3132021216).

The authors also thank Dr. Hao Fu, Dr. Binbin Ying, and Jun Li for valuable discussions and suggestions.

Conflict of Interest

The authors declare no conflict of interest.

Author Contributions

R.P. and Y.P. contributed equally to this work. R.P. and X.L. generated the ideas and wrote the paper; R.P. and Y.P. built up and ran the numerical simulation models, fabricated, and characterized the devices and collected the data; Z.L. synthesized the MWCNT samples and assisted in Raman testing; B.L. and Z.Q. developed and optimized the HIV-1 testing protocol; P.P. and S.Z. did imaging and data analysis; A.R.W., X.S.T., and X.L. coordinated and supervised this project.

Data Availability Statement

The data that supports the findings of this study are available in the supplementary material of this article, additional data are available from the authors upon reasonable request.

Keywords

carbon nanotube (CNT), ionic current rectification, ionic diode, ionotronics, nanofluidics

Received: January 20, 2021
Revised: April 27, 2021
Published online: June 25, 2021

[1] Y. Feng, W. Zhu, W. Guo, L. Jiang, *Adv. Mater.* **2017**, *29*, 1702773.
[2] R. Li, X. Fan, Z. Liu, J. Zhai, *Adv. Mater.* **2017**, *29*, 1702983.
[3] H. C. Yang, Y. Xie, J. Hou, A. K. Cheetham, V. Chen, S. B. Darling, *Adv. Mater.* **2018**, *30*, 1801495.
[4] M. Wang, Y. Hou, L. Yu, X. Hou, *Nano Lett.* **2020**, *20*, 6937.
[5] Y. Tian, L. Wen, X. Hou, G. Hou, L. Jiang, *ChemPhysChem* **2012**, *13*, 2455.
[6] I. Vlassiouk, T. R. Kozel, Z. S. Siwy, *J. Am. Chem. Soc.* **2009**, *131*, 8211.
[7] B. Corry, *Energy Environ. Sci.* **2011**, *4*, 751.
[8] E. O. Gabrielsson, K. Tybrandt, M. Berggren, *Lab Chip* **2012**, *12*, 2507.
[9] J. H. Han, K. B. Kim, H. C. Kim, T. D. Chung, *Angew. Chem., Int. Ed.* **2009**, *48*, 3830.
[10] M. Ali, S. Mafe, P. Ramirez, R. Neumann, W. Ensinger, *Langmuir* **2009**, *25*, 11993.
[11] J. Cervera, P. Ramirez, S. Mafe, P. Stroeve, *Electrochim. Acta* **2011**, *56*, 4504.
[12] J. Gao, W. Guo, D. Feng, H. Wang, D. Zhao, L. Jiang, *J. Am. Chem. Soc.* **2014**, *136*, 12265.
[13] Y. Liu, L. Yobas, *Nano Lett.* **2014**, *14*, 6983.
[14] B. R. Putra, E. Madrid, L. Tshwenya, O. A. Arotiba, F. Marken, *Desalination* **2020**, *480*, 114351.
[15] C. Yang, Z. Suo, *Nat. Rev. Mater.* **2018**, *3*, 125.
[16] G. Nguyen, I. Vlassiouk, Z. S. Siwy, *Nanotechnology* **2010**, *21*, 265301.
[17] X. Huang, X. Y. Kong, L. Wen, L. Jiang, *Adv. Funct. Mater.* **2018**, *28*, 1801079.
[18] I. Vlassiouk, Z. S. Siwy, *Nano Lett.* **2007**, *7*, 552.
[19] J. Y. Jung, P. Joshi, L. Petrossian, T. J. Thornton, J. D. Posner, *Anal. Chem.* **2009**, *81*, 3128.
[20] E. Choi, C. Wang, G. T. Chang, J. Park, *Nano Lett.* **2016**, *16*, 2189.
[21] J. Cervera, B. Schiedt, R. Neumann, S. Mafá, P. Ramírez, *J. Chem. Phys.* **2006**, *124*, 104706.
[22] Y. Qiu, Z. S. Siwy, M. Wanunu, *Anal. Chem.* **2019**, *91*, 996.
[23] L. Wang, Y. Yan, Y. Xie, L. Chen, J. Xue, S. Yan, Y. Wang, *Phys. Chem. Chem. Phys.* **2011**, *13*, 576.
[24] J. M. Perry, K. Zhou, Z. D. Harms, S. C. Jacobson, *ACS Nano* **2010**, *4*, 3897.
[25] K. Xiao, P. Li, G. Xie, Z. Zhang, L. Wen, L. Jiang, *RSC Adv.* **2016**, *6*, 55064.
[26] E. C. Yusko, R. An, M. Mayer, *ACS Nano* **2010**, *4*, 477.
[27] G. Xie, K. Xiao, Z. Zhang, X. Y. Kong, Q. Liu, P. Li, L. Wen, L. Jiang, *Angew. Chem., Int. Ed.* **2015**, *54*, 13664.
[28] L. Wang, Y. Feng, Y. Zhou, M. Jia, G. Wang, W. Guo, L. Jiang, *Chem. Sci.* **2017**, *8*, 4381.
[29] K. Mathwig, B. D. B. Aaronson, F. Marken, *ChemElectroChem* **2018**, *5*, 897.
[30] X. Zhang, Q. Wen, L. Wang, L. Ding, J. Yang, D. Ji, Y. Zhang, L. Jiang, W. Guo, *ACS Nano* **2019**, *13*, 4238.
[31] X. Zhu, J. Hao, B. Bao, Y. Zhou, H. Zhang, J. Pang, Z. Jiang, L. Jiang, *Sci. Adv.* **2018**, *4*, eaau1665.
[32] O. J. Cayre, T. C. Suk, O. D. Velev, *J. Am. Chem. Soc.* **2007**, *129*, 10801.
[33] B. Riza Putra, M. Carta, R. Malpass-Evans, N. B. McKeown, F. Marken, *Electrochim. Acta* **2017**, *258*, 807.
[34] H. J. Koo, S. T. Chang, O. D. Velev, *Small* **2010**, *6*, 1393.
[35] Y. Rong, Q. Song, K. Mathwig, E. Madrid, D. He, R. G. Niemann, P. J. Cameron, S. E. C. Dale, S. Bending, M. Carta, R. Malpass-Evans, N. B. McKeown, F. Marken, *Electrochem. Commun.* **2016**, *69*, 41.
[36] Y. Zhou, Y. Hou, Q. Li, L. Yang, Y. Cao, K. H. Choi, Q. Wang, Q. M. Zhang, *Adv. Mater. Technol.* **2017**, *2*, 1700118.
[37] Z. Zhang, X. Y. Kong, K. Xiao, G. Xie, Q. Liu, Y. Tian, H. Zhang, J. Ma, L. Wen, L. Jiang, *Adv. Mater.* **2016**, *28*, 144.
[38] Z. Zhang, X. Y. Kong, K. Xiao, Q. Liu, G. Xie, P. Li, J. Ma, Y. Tian, L. Wen, L. Jiang, *J. Am. Chem. Soc.* **2015**, *137*, 14765.
[39] W. Zhang, X. Zhang, C. Lu, Y. Wang, Y. Deng, *J. Phys. Chem. C* **2012**, *116*, 9227.
[40] Y. Kong, X. Fan, M. Zhang, X. Hou, Z. Liu, J. Zhai, L. Jiang, *ACS Appl. Mater. Interfaces* **2013**, *5*, 7931.
[41] L. J. Cheng, L. J. Guo, *ACS Nano* **2009**, *3*, 575.
[42] K. Xiao, L. Chen, G. Xie, P. Li, X. Y. Kong, L. Wen, L. Jiang, *Nanoscale* **2018**, *10*, 6850.
[43] R. Yan, W. Liang, R. Fan, P. Yang, *Nano Lett.* **2009**, *9*, 3820.
[44] K. Xiao, G. Xie, Z. Zhang, X. Y. Kong, Q. Liu, P. Li, L. Wen, L. Jiang, *Adv. Mater.* **2016**, *28*, 3345.
[45] S. Z. Bisri, S. Shimizu, M. Nakano, Y. Iwasa, *Adv. Mater.* **2017**, *29*, 1607054.
[46] H. Chun, T. D. Chung, *Annu. Rev. Anal. Chem.* **2015**, *8*, 441.
[47] Z. Zhang, L. Wen, L. Jiang, *Chem. Soc. Rev.* **2018**, *47*, 322.
[48] J. P. Hsu, H. H. Wu, C. Y. Lin, S. Tseng, *Anal. Chem.* **2017**, *89*, 3952.
[49] H. Verweij, M. C. Schillo, J. Li, *Small* **2007**, *1178*, 1996.
[50] R. H. Tunuguntla, R. Y. Henley, Y. C. Yao, T. A. Pham, M. Wanunu, A. A. Noy, R. H. Tunuguntla, R. Y. Henley, Y. C. Yao, T. A. Pham, M. Wanunu, A. A. Noy, *Science* **2017**, *357*, 792.
[51] M. Whitby, N. Quirke, *Nat. Nanotechnol.* **2007**, *2*, 87.
[52] E. Secchi, S. Marbach, A. Niguès, D. Stein, A. Siria, L. Bocquet, *Nature* **2016**, *537*, 210.
[53] F. Fornasiero, H. G. Park, J. K. Holt, M. Stadermann, C. P. Grigoropoulos, A. Noy, O. Bakajin, *Proc. Natl. Acad. Sci. USA* **2008**, *105*, 17250.
[54] M. Wang, Z. Sheng, X. Hou, Y. Zhang, D. Wang, H. Meng, B. Chen, K. Zhan, Y. Yin, P. Stroeve, *Adv. Mater.* **2019**, *31*, 1805130.

[55] S. E. Moya, A. Ilie, J. S. Bendall, J. L. Hernandez-Lopez, J. Ruiz-García, W. T. S. Huck, *Macromol. Chem. Phys.* **2007**, *208*, 603.
[56] K. A. Williams, P. T. M. Veenhuizen, B. G. de la Torre, R. Eritja, C. Dekker, *Nature* **2002**, *420*, 761.
[57] N. R. Scruggs, J. W. F. Robertson, J. J. Kasianowicz, K. B. Migler, *Nano Lett.* **2009**, *9*, 3853.
[58] J. Wu, X. Zhan, B. J. Hinds, *Chem. Commun.* **2012**, *48*, 7979.
[59] R. Peng, Y. Pan, Z. Li, S. Zhang, A. R. Wheeler, X. Tang, X. Liu, *Adv. Funct. Mater.* **2020**, *30*, 2003177.
[60] Y. Ma, J. Guo, L. Jia, Y. Xie, *ACS Sens.* **2018**, *3*, 167.
[61] H. Daiguji, Y. Oka, K. Shirono, *Nano Lett.* **2005**, *5*, 2274.
[62] Z. Yuan, A. L. Garcia, G. P. Lopez, D. N. Petsev, *Electrophoresis* **2007**, *28*, 595.
[63] R. Peng, X. S. Tang, D. Li, *Small* **2018**, *14*, 1800013.
[64] X. Zhang, H. Chen, H. Zhang, *Chem. Commun.* **2007**, 1395.
[65] D. G. Haywood, Z. D. Harms, S. C. Jacobson, *Anal. Chem.* **2014**, *86*, 11174.
[66] R. Peng, D. Li, *Nanoscale* **2016**, *8*, 12237.
[67] S. Pennathur, J. G. Santiago, *Anal. Chem.* **2005**, *77*, 6782.
[68] I. Vlassiouk, S. Smirnov, Z. Siwyt, *Nano Lett.* **2008**, *8*, 1978.
[69] I. Vlassiouk, S. Smimov, Z. Siwy, *ACS Nano* **2008**, *2*, 1589.
[70] C. Y. Lin, L. H. Yeh, Z. S. Siwy, *J. Phys. Chem. Lett.* **2018**, *9*, 393.
[71] P. Krishnakumar, P. B. Tiwari, S. Staples, T. Luo, Y. Darici, J. He, S. M. Lindsay, *Nanotechnology* **2012**, *23*, 455101.
[72] D. Li, *Electrokinetics in Microfluidics*, Academic Press, San Diego, CA **2004**.
[73] D. Ji, Q. Wen, L. Cao, Q. Kang, S. Lin, X. Zhang, L. Jiang, W. Guo, *Adv. Mater. Technol.* **2019**, *4*, 1800742.
[74] F. Yan, L. Yao, Q. Yang, K. Chen, B. Su, *Anal. Chem.* **2019**, *91*, 1227.
[75] J. Feng, M. Graf, K. Liu, D. Ovchinnikov, D. Dumcenco, M. Heiranian, V. Nandigana, N. R. Aluru, A. Kis, A. Radenovic, *Nature* **2016**, *536*, 197.
[76] W. Chen, Q. Wang, J. Chen, Q. Zhang, X. Zhao, Y. Qian, C. Zhu, L. Yang, Y. Zhao, X. Y. Kong, B. Lu, L. Jiang, L. Wen, *Nano Lett.* **2020**, *20*, 5705.
[77] Y. Teng, X. Y. Kong, P. Liu, Y. Qian, Y. Hu, L. Fu, W. Xin, L. Jiang, L. Wen, *Nano Res.* **2020**, *14*, 1421.
[78] V. Schroeder, S. Savagatrup, M. He, S. Lin, T. M. Swager, *Chem. Rev.* **2019**, *119*, 599.
[79] T. C. Granade, M. Kodani, S. K. Wells, A. S. Youngpairoj, S. Masciotra, K. A. Curtis, S. Kamili, S. M. Owen, *J. Virol. Methods* **2018**, *259*, 60.
[80] M. Mazloumi, S. Shadmehr, Y. Rangom, L. F. Nazar, X. S. Tang, *ACS Nano* **2013**, *7*, 4281.